Shock Wave Interaction with a Thermal Layer

D. Rayevsky*
New York University, New York, New York 10003
and
G. Ben-Dor†
Ben-Gurion University of the Negev, Beer Sheva, Israel

Introduction

ALTHOUGH a general discussion of the nature of the interaction of a moving planar shock wave over a thin thermal layer was given more than three decades ago by Hess,[1] the interest in this phenomenon has been recently revived because it can help to better understand the propagation of nuclear-burst-generated spherical blast waves over the baked-ground surface.

Experimental investigations of the interaction of relatively weak moving planar shock waves with thin thermal layers were reported in Refs. 2–4. Numerical simulations of the interaction under consideration were reported more recently in Refs. 5–7.

Mirels[8] presented an analytical model for the interaction between a moving shock wave and a thin thermal layer of semi-infinite extent. His model was based on flowfield characteristics that were deduced from the numerical calculations of Schneyer and Wilkins.[5] Mirels'[8] model was quite capable of predicting the peak surface (stagnation) pressure, the forward extent of the shock-induced precursor, and the surface pressure behind the precursor.

A schematic illustration of the problem at hand, at $t = 0$ (i.e., the instant the shock wave reaches the leading edge of the thermal layer that is located at $x = 0$), is shown in Fig. 1a. The planar shock wave, having a velocity V_s, propagates from right to left in a laboratory coordinate system along a stationary wall, i.e., $V_W = 0$. The domain ahead of it is divided into two regions: region 1 is outside and region 4 is inside the semi-infinite thermal layer of height h. The flows both outside and inside the thermal layer are at rest, i.e., $V_1 = V_4 = 0$. In addition, $P_4 = P_1$ and $T_4 > T_1$ where P and T are the static pressure and temperature, respectively. The shock-induced flow, region 2, has a velocity of V_2.

The same problem in shock fixed coordinates is shown in Fig. 1b. Now the flows outside (state 1) and inside (state 4) the thermal layer and the surface move toward the stationary shock wave (i.e., $u_s = 0$) with velocities $u_1 = u_4 = u_w = V_s$, and the flow velocity behind the shock wave is $u_2 = V_s - V_2$.

It is well known that after the initial transient is over the interaction can be characterized as either separated or unseparated, depending on the incident shock wave Mach number $M_s = V_s/a_1$ and the acoustic impedance ratio $\rho_4 a_4/\rho_1 a_1$ (ρ is the density and a the local speed of sound).

Figure 2 illustrates the domains of separated and unseparated flows in the (M_1, A_{41}) plane, where $M_1 = u_1/a_1$ (i.e., $M_1 = M_s$) and $A_{41} = a_4/a_1$. It is evident from Fig. 2 that the boundary line between the separated and the unseparated flows depends also on the ratios of the specific heat capacities outside and inside the thermal layer (γ_1 and γ_4, respectively).

The flow patterns corresponding to unseparated and separated interactions are also shown schematically in Fig. 2. These flows are steady and unsteady, respectively, in incident shock fixed coordinates. Although in the former case the triple point T continuously moves away from the surface, it attains a constant distance from the surface and remains there in the latter one. However, inviscid numerical simulations indicated that separate flow patterns have a self-similar nature once the triple point exceeds a height of about $(1.5 \div 2)\ h$. Thus, in a laboratory coordinate system, the triple-point trajectory is a straight line. The inviscid numerical simulations further revealed that the triple-point trajectory angle depends on the incident shock wave Mach number M_s and the ratio of the acoustic impedances $\rho_4 a_4/\rho_1 a_1$. However, due to the separation of the flow, the values of the Reynolds numbers under the triple point are relatively small. Hence, it seems unjustified to neglect viscous effects. Consequently, we have initiated a numerical investigation of the influence of viscosity on the triple-point trajectory. The results are reported in the following.

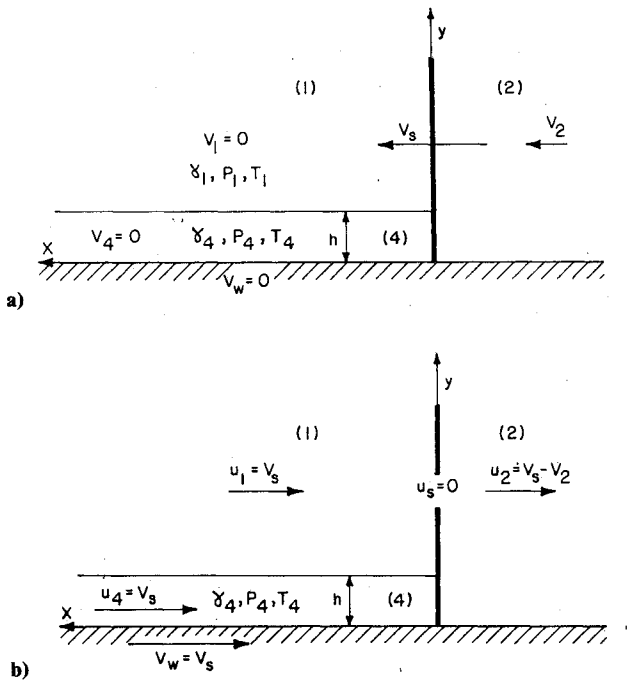

Fig. 1 Schematic illustration of the problem under consideration in a) a laboratory frame of reference and b) shock fixed coordinates.

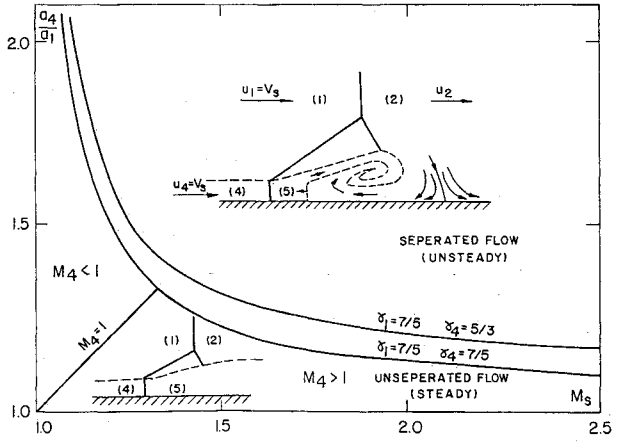

Fig. 2 Domains of separated and unseparated interactions.

Received Jan. 7, 1991; revision received June 30, 1991; accepted for publication July 17, 1991.

*Research Scientist, Courant Institute of Mathematical Sciences.
†Professor, Pearlstone Center for Aeronautical Engineering Studies, Department of Mechanical Engineering.

Numerical Method

To numerically simulate the viscous interaction of a planar shock wave with a thermal layer, the idea of numerical viscosity was adopted. The numerical viscosity is inherent in the finite difference equations of inviscid gas motion. It is shown in Ref. 9, where some explicit algorithms were investigated by analyzing the terms on the right-hand side of the conservation equations, that second-order schemes have a dominating term of the form $F_v = (\partial/\partial x)[(\partial^2 u/\partial x^2)]$, which plays a role of numerical (not artificial) viscosity. This term arises from the fact that the replacement of the exact derivatives of the gas dynamic equations by finite differences results in remainder terms of the $m + 1$ order, where m is the scheme's order of accuracy. A detailed analysis of the remainder terms for different algorithms (including MacCormack's) was conducted by Shokin.[9] In the following, only the basic idea is illustrated. Second-order algorithms approximate the first derivatives as follows

$$\frac{df}{dx} \approx \frac{f_{k+1} - f_{k-1}}{2\Delta x} \tag{1}$$

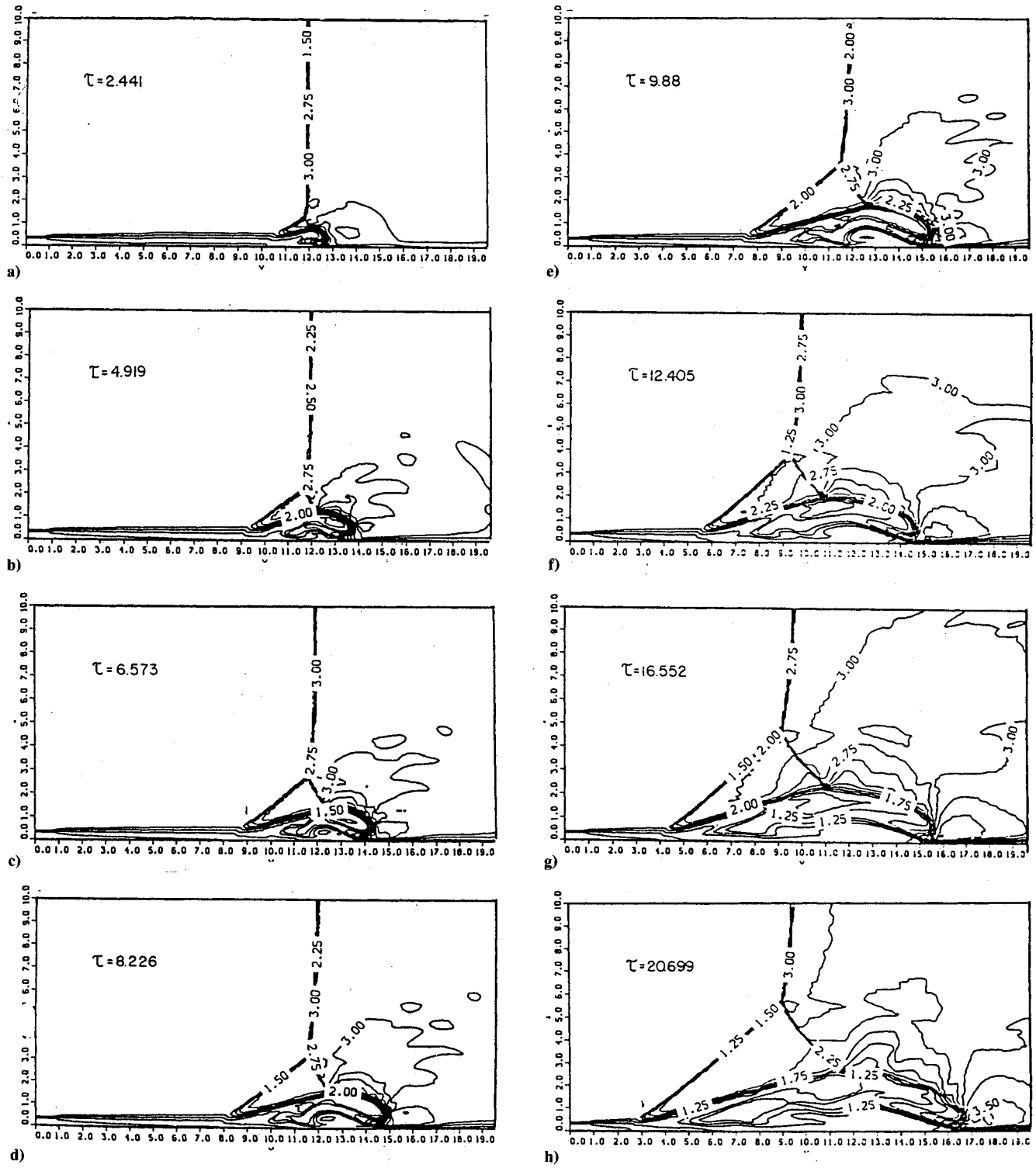

Fig. 3 Evolution of the waves configuration for $M_S = 2.0$, $\rho_4/\rho_1 = 0.2$, and $h = 0.35$ cm: a) $\tau = 2.441$; b) $\tau = 4.919$; c) $\tau = 6.573$; d) $\tau = 8.226$; e) $\tau = 9.88$; f) $\tau = 12.405$; g) $\tau = 16.522$; h) $\tau = 20.699$.

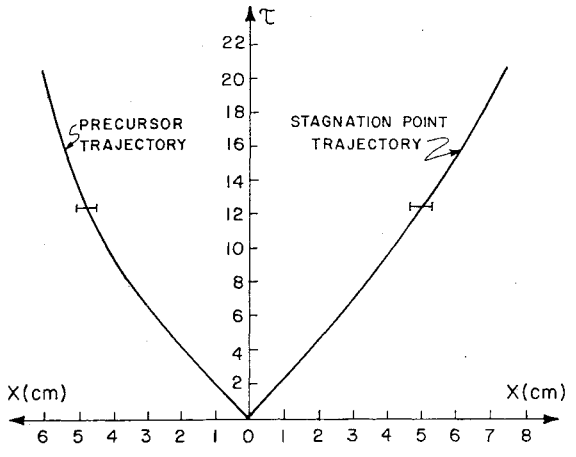

Fig. 4 Trajectories of the precursor and the stagnation point for the case shown in Fig. 3.

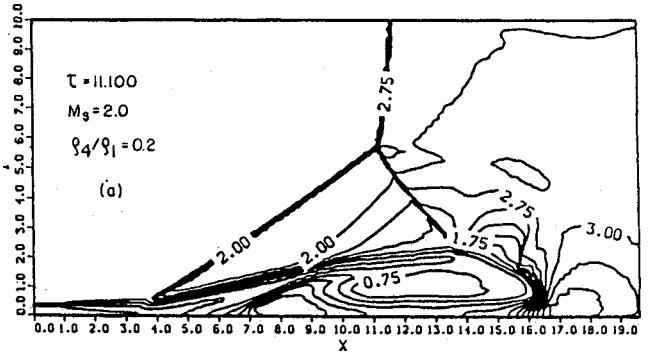

a)

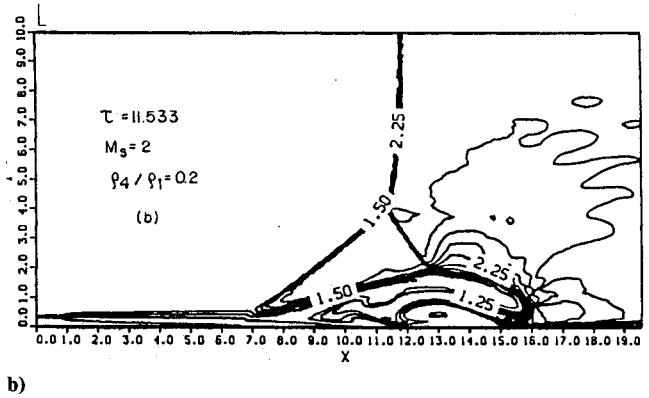

b)

Fig. 5 Comparison of the wave structures for $M_s = 2.0$, $\rho_4/\rho_1 = 0.2$, and $h = 0.35$ cm: a) inviscid; b) viscous.

Expanding f^n_{k+1} and f^n_{k-1} about the point k and substituting these expansions into Eq. (1) yields

$$\frac{f_{k+1}-f_{k-1}}{2\Delta x} = \frac{df}{dx} + \sum_{n=1}^{\infty} \frac{d^{2n+1}f_k}{dx^{2n+1}} \frac{h^{2n}}{(2n+1)!} \tag{2}$$

Defining the remainder part in Eq. (2) as F_v finally results in

$$\frac{f_{k+1}-f_{k-1}}{2\Delta x} = \frac{df}{dx} + F_v \tag{3}$$

Hence, one can see from Eq. (3) that the replacement of the analytical derivative df/dx by the finite difference $(f_{k+1} - f_{k-1})/2\Delta x$ leaves some extra terms, which are known as numerical viscosity. The coefficients of these terms are nonlinear and they depend on the numerical algorithm.

If the no-slip boundary condition is imposed along the surface, i.e., $u(x,y = 0) = 0$ and $v(x,y = 0) = 0$, then the previously mentioned F_v term results in a boundary layer that is analogous to the kinematic boundary layer as long as $Re \leq 10^5$. This "numerical" force is of course mesh dependent. For s hock tube simulations having approximately a 10-cm scale and a few hundred grid points in each direction, F_v provides the width of a shock wave ($\sim 10^{-4}$ m). This value corresponds to flows with $Re \sim 10^5$.

To verify this idea of numerical viscosity, the interaction of a head-on reflected shock wave with an incident shock-induced boundary layer was investigated recently by Lyakhov[10] using the idea of numerical viscosity. His numerical results resembled very good agreement with experimental data.

Furthermore, Lyakhov's numerical investigation revealed that, when the boundary layer separates due to its interaction with a shock wave that reflects from the end wall, the shear stress along the surface is more dominant than viscous dissipation in the separated flow region above the vortex and below the triple point.

The present numerical code was upstream oriented and based on the second-order MacCormack[11] algorithm coupled with simplified flux-corrected transport (FCT).[12]

In the two-dimensional case, the code has the following predictor-corrector form for calculating $A^{n+1}_{k,l}$ from $A^n_{k,l}$ where $A^n_{k,l} = A(n\Delta t, k\Delta x, l\Delta y)$:

$$\tilde{A}_{k,l} = A^n_{k,l} - \frac{\Delta t}{\Delta x}\delta^+_k B^n_{k,l} - \frac{\Delta t}{\Delta y}\delta^+_l C_{k,l}$$

$$A^{n+1}_{k,l} = \frac{1}{2}\left[A^n_{k,l} + \tilde{A}_{k,l} - \frac{\Delta t}{\Delta x}\delta^-_k \tilde{B}_{k,l} - \frac{\Delta t}{\Delta y}\delta^-_l \tilde{C}_{k,l}\right]$$

where

$$\delta^+_k = f_{k+1} - f_k, \qquad \delta^-_k = f_k - f_{k-1}$$

A nonpermeable wall with a no-slip condition at the surface was used as a boundary condition. The basic nondimensionalizing scales for the velocity, length, and time were, respectively,

$$\bar{V} = \sqrt{p_1/\rho_1}, \qquad \bar{L} = 1 \text{ cm}, \qquad \bar{t} = \bar{L}/\bar{V}$$

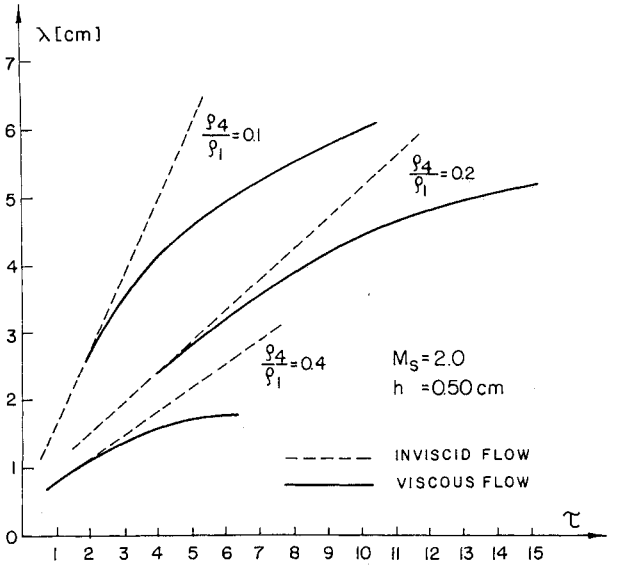

Fig. 6 Dependence of the triple-point trajectory on the densities ratio—ρ_4/ρ_1 for inviscid and viscous interaction and $M_s = 2.0$ and $h = 0.50$ cm. (Note that since M_s = const in this figure, the τ axis can be simply transformed to real distances.)

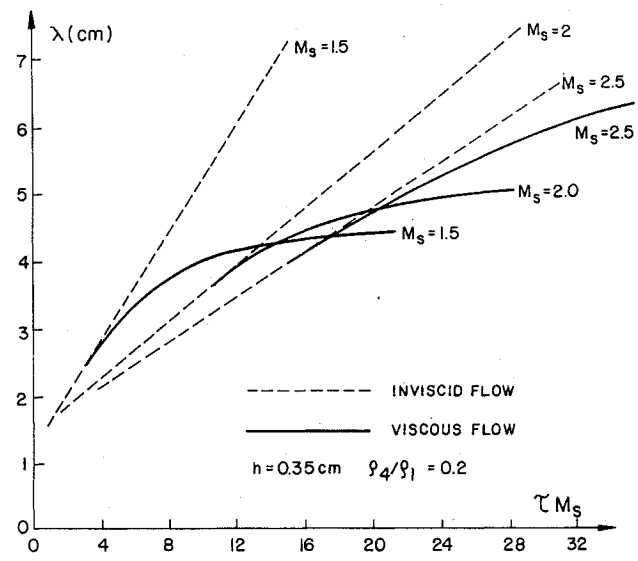

Fig. 7 Dependence of the triple-point trajectory on the shock wave Mach number M_s for inviscid and viscous interactions and $\rho_4/\rho_1 = 0.2$ and $h = 0.35$ cm.

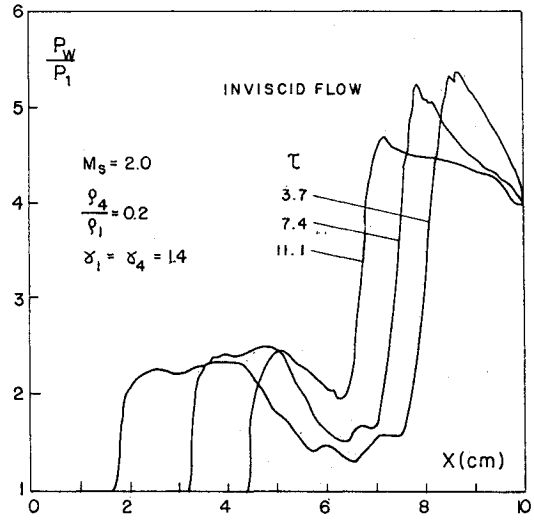

Fig. 8 Pressure distributions along the wall surface for an inviscid interaction ($M_s = 2.0$, $\rho_4/\rho_1 = 0.2$) at three different times.

Basic Equations

The unsteady conservation equations of a compressible inviscid gas were solved in shock fixed coordinates. As mentioned earlier, viscous effects were accounted for by means of the implicitly existing viscous term F_v. Thus, the system of equations was

$$\frac{\partial A}{\partial t} + \frac{\partial B}{\partial x} + \frac{\partial C}{\partial y} = 0 \tag{4a}$$

where

$$A = \begin{bmatrix} \rho \\ \rho u \\ \rho v \\ \rho e \end{bmatrix}, \quad B = \begin{bmatrix} \rho u \\ \rho u^2 + p + F_v \\ \rho uv \\ (\rho e + p + F_v)u \end{bmatrix},$$

$$C = \begin{bmatrix} \rho v \\ \rho uv \\ \rho v^2 + p + F_v \\ (\rho e + p + F_v)v \end{bmatrix} \tag{4b}$$

where ρ u, v, p, and e are density, x and y components of the gas velocity, pressure, and total (internal and kinetic) energy per volume, respectively. The energy per volume is defined as

$$e = \epsilon + (q^2/2)$$

where the internal energy ϵ is calculated from

$$\epsilon = (1/\gamma - 1)(p/\rho)$$

i.e., the equation of state of a perfect gas and the velocity q is obtained from

$$q^2 = u^2 + v^2$$

Results and Discussion

The evaluation of the flowfield associated with the interaction of a planar shock wave with a thermal layer is shown in Figs. 3a–3h for eight different values of τ, where τ is a nondimensional time, i.e., $\tau = t/\bar{t}$. Thus, the real time can be calculated from

$$t = \tau \cdot \bar{t} = \tau \frac{L}{\sqrt{p_1/\rho_1}}$$

The results shown in Figs. 3 are for air both in regions 1 and 4 and the following conditions: $M_s = 2$, $h = 0.35$ mm, $p_4 = p_1 = 1$ atm, $T_1 = 288$ K, and $\rho_4/\rho_1 = 0.2$. Based on these conditions, the real time is related to the nondimensional time in the following way t[s] $= 34 \times 10^{-6}\tau$. In addition, the results shown in Fig. 3 account for viscous effects. The CPU time required for a typical computation was about 7000 s on a CDC Cyber 840 computer.

It is evident from Figs. 3a–3h that the entire structure grows with time. Furthermore, as the structure grows, more details of the interaction become visible.

The distance to which the precursor and the stagnation point propagated are shown in Fig. 4. It is evident that the forward propagation of the precursor is slower than that of the backward propagation of the stagnation point. However, both of the trajectories indicate that the precursor and the stagnation point approach asymptotically a fixed location.

A comparison of the flowfield structure between two calculations, one with and one without viscosity, is shown in Fig. 5. Although there is a slight difference between the times of these two calculations, it is evident that the structure of the interaction is much larger when the flow is assumed to be inviscid (see Fig. 5a). Although for the inviscid case, shown in Fig. 5a, the triple-point height λ is about 5.7 cm at $\tau = 11.100$ ($t = 377.4$ μs), it is only about 4.25 cm at a slightly later time $\tau = 11.533$

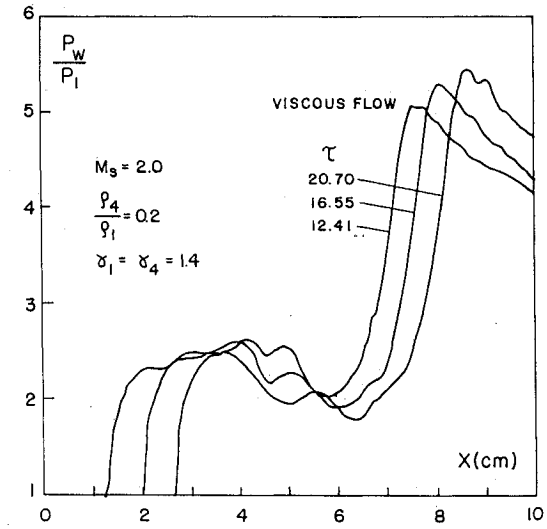

Fig. 9 Pressure distributions along the wall surface for a viscous interaction ($M_s = 2.0$, $\rho_4/\rho_1 = 0.2$) at three different times.

($t = 392$ μs) when the viscous effects are accounted for (see Fig. 5b). This is because viscous effects can be thought of as a mechanism that introduces suction into the flowfield along the wall. Consequently, the amount of fluid trapped under the bifurcated shock is smaller when viscous effects are accounted for. It is also important to note that although in an inviscid case (Fig. 5a), a clear stagnation point is evident behind the vortex, in the viscous case (Fig. 5b), a clear boundary layer is seen to develop along the wall behind the vortex.

It is also evident from Figs. 5a and 5b that although the precursor precedes the shock wave by about 7.8 cm when the fluid is assumed to be inviscid, the precursor is only 4.3 cm ahead of the shock wave for the viscous case.

The stagnation point, on the other hand, lags about 5 and 4.2 cm behind the shock wave in the inviscid and viscous cases, respectively.

The dependence of the triple-point trajectory on the densities ratio ρ_4/ρ_1 for both viscous and inviscid fluids is shown in Fig. 6 for a fixed shock wave Mach number $M_s = 2$.

Figure 6 indicates the following:

1) For an inviscid fluid, the triple-point trajectory is a straight line.

2) For a viscous fluid, the triple-point trajectory approaches a constant height.

3) The triple point is higher when the fluid is assumed to be inviscid.

4) The smaller ρ_4/ρ_1 is, the higher the triple-point height. Recall that since $P_4 = P_1$, i.e., $P_4/P_1 = 1$, $T_1/T_4 = \rho_4/\rho_1$, smaller values of ρ_4/ρ_1 are equivalent to larger values of T_4/T_1, i.e., higher temperatures inside the thermal layer.

The dependence of the triple-point trajectory on the shock wave Mach number M_s for both viscous and inviscid fluids is shown in Fig. 7 for a fixed value of $\rho_4/\rho_1 = 0.2$. It is again evident that the triple-point trajectories are straight when the fluid is assumed to be inviscid. However, when viscosity is accounted for, then the triple-point trajectories approach an asymptotic level.

The pressure distributions along the surface for an inviscid and a viscous case are shown in Figs. 8 and 9, respectively. The maximum pressure along the surface is obtained at the stagnation point behind the shock wave. As shown in Fig. 8, the stagnation pressure increases from about $P_{4st} = 4.69\ P_1$ at $\tau = 3.7$ ($t = 125.8$ μs) to about $P_{4st} = 5.24\ P_1$ at $\tau = 7.4$ ($t = 251.6$ μs) and finally to about $P_{4st} = 5.37\ P_1$ at $\tau = 11.1$ ($t = 377.4$ μs). This trend might suggest that the stagnation pressure approaches an asymptotic value.

When viscous effects are accounted for (see Fig. 9), the stagnation pressure increases from about $P_{4st} = 5.10\ P_1$ at $\tau = 12.41$ ($t = 421.9$ μs) to about $P_{4st} = 5.29\ P_1$ at $\tau = 16.55$ ($t = 562.7$ μs) and finally to about $P_{4st} = 5.41\ P_1$ at $\tau = 20.70$ ($t = 703.8$ μs). Unlike the case of an inviscid fluid, it cannot be concluded from these values that an asymptotic stagnation pressure is approached. This is in spite of the fact that the viscous calculations shown in Fig. 9 extend to 703.8 μs after the interaction started, whereas the inviscid calculations shown in Fig. 8 extend only to 377.4 μs.

Note that Figs. 8 and 9 imply that the so-called stagnation point moves along the surface in the x direction. The horizontal velocity of the stagnation point seems to be larger when the fluid is assumed to be inviscid.

Furthermore, although for both the viscous and the inviscid calculations the horizontal velocity of the stagnation point seems to be constant, the horizontal velocity of the leading edge of the precursor seems to be increasing, i.e., the leading edge of the precursor seems to be accelerating. Note in Fig. 8 that although in the first time interval of $\Delta\tau = 3.7$ ($\Delta t = 125.8$ μs) the precursor propagated a distance of 1.18 cm, in the second time interval of $\Delta\tau = 3.7$, the precursor advanced about 1.49 cm, i.e., its average velocity increased about 26%. Similarly, for the viscous case (Fig. 9) in the first time interval of $\Delta\tau = 4.14$ ($\Delta t = 140.76$ μs) the precursor propagated about 0.625 cm, whereas in the second time interval of $\Delta\tau = 4.15$ ($\Delta t = 141.1$ μs), it propagated a distance of about 0.729 cm. This difference implies an increase of about 16% in the average velocity of the precursor.

Acknowledgment

The authors would like to thank the Pearlstone Center for Aeronautical Engineering Studies for financially supporting D. Rayevsky's stay in the Department of Mechanical Engineering of the Ben-Gurion University of the Negev.

References

[1]Hess, R. V., "Interaction of Moving Shocks and Hot Layers," NACA TN 4002, 1957.

[2]Griffith, W. C., "Interaction of a Shock Wave with a Thermal Boundary Layer," *Journal of Aeronautical Sciences,* Vol. 23, No. 1, 1956 pp. 16-22.

[3]Gion, E. J., "Plane Shock Interacting with Thermal Layer," *Physics of Fluids,* Vol. 20, No. 4, 1977, pp. 700-702.

[4]Reichenbach, H., "Roughness and Heated Layer Effects on Shock Wave Propagation and Reflection—Experimental Results," Ernst Mach Inst., Freiburg, Germany, Rept. E24/85, 1985.

[5]Schneyer, G. P., and Wilkins, D. E., "Thermal Layer-Shock Interaction (Precursor) Simulation Data Book," S-Cubed, Rept. SSS-R-84-6584, Albuquerque, NM, 1984.

[6]Glowacki, W. S., Kuhl, A. L., Glaz, H. M., and Ferguson, R. E., "Shock Wave Interaction with High Sound Speed Layers," *Shock Waves and Shock Tubes,* edited by D. Bershader and R. Hanson, Stanford Univ. Press, Berkeley, CA, 1986, pp. 187-194.

[7]Fry, M., and Book, D. L., "Shock Dynamics in Heated Layers," *Shock Waves and Shock Tubes,* edited by D. Bershader and R. Hanson, Stanford Univ. Press, Berkeley, CA, 1986, pp. 517-522.

[8]Mirels, H., "Interaction of Moving Shock with Thin Stationary Thermal Layer," *Shock Tubes and Waves,* edited by H. Gronig, VCH, Weinheim, Germany, 1988, pp. 177-183.

[9]Shokin, Yu. I., *A Method of Differential Approximation,* Novosibirsk, Nauke, Russia, 1979 (in Russian).

[10]Lyakhov, V. N., private communication, 1990.

[11]MacCormack, R. W., "The Effect of Viscosity on Hypervelocity Impact Cratering," AIAA Paper 69-354, 1969.

[12]Boris, J., and Book, D., "Flux-Corrected Transport: I SHASTA, A Fluid Transport Algorithm that Works," *Journal of Computational Physics,* Vol. 11, 1973, pp. 38-44.

Frequency Analysis of Axially Loaded Structures

C. Sundararajan*
Houston, Texas 77396

Introduction

NATURAL frequencies of axially loaded beams, plates, shells, and other types of components are often required in the design of aerospace structures. Changes in the location of masses such as instruments, equipment, and other attachments that add to the mass of structures without contributing significantly to structural stiffness do affect the natural frequencies. Axial loads, if sufficiently high, also affect the natural frequencies. Hence, design engineers are interested in the effect of alterations in mass distributions and axial loads on the natural frequencies in order to obtain optimal or near-optimal structural design by using an ideal combination of mass distribution and axial load. Repeated frequency analyses of the structure with various combinations of mass distributions and axial loads is an expensive and time-consuming process. If, however, a simple procedure were available to study the

Received Aug. 29, 1989; revision received Feb. 17, 1990; accepted for publication March 6, 1990.

*Consultant, 10723 Thorncliff Drive.